



# Pia-FLOW: Deciphering hemodynamic maps of the pial vascular connectome and its response to arterial occlusion

Chaim Glück<sup>a,b,1</sup> , Quanyu Zhou<sup>a,c,1</sup> , Jeanne Droux<sup>b,d</sup>, Zhenyue Chen<sup>a,c</sup> , Lukas Glandorf<sup>a,c</sup> , Susanne Wegener<sup>b,d</sup> , Daniel Razansky<sup>a,b,c</sup>, Bruno Weber<sup>a,b,2</sup>, and Mohamad El Amki<sup>b,d,2</sup>

Affiliations are included on p. 9.

Edited by Mark Nelson, University of Vermont, Burlington, VT; received February 7, 2024; accepted June 4, 2024

The pial vasculature is the sole source of blood supply to the neocortex. The brain is contained within the skull, a vascularized bone marrow with a unique anatomical connection to the brain meninges. Recent developments in tissue clearing have enabled detailed mapping of the entire pial and calvarial vasculature. However, what are the absolute flow rate values of those vascular networks? This information cannot accurately be retrieved with the commonly used bioimaging methods. Here, we introduce Pia-FLOW, a unique approach based on large-scale transcranial fluorescence localization microscopy, to attain hemodynamic imaging of the whole murine pial and calvarial vasculature at frame rates up to 1,000 Hz and spatial resolution reaching 5.4  $\mu\text{m}$ . Using Pia-FLOW, we provide detailed maps of flow velocity, direction, and vascular diameters which can serve as ground-truth data for further studies, advancing our understanding of brain fluid dynamics. Furthermore, Pia-FLOW revealed that the pial vascular network functions as one unit for robust allocation of blood after stroke.

blood vessels | stroke | physiology | cerebral blood flow

Unlike other organs such as the liver or kidney, the brain is vascularized from outside where most large cerebral arteries lie horizontally above the cortical surface within the subarachnoid space (pia) (1). The pial vascular network is of utmost importance, as it is the only source of blood supply to the neocortex and a key contributor to cerebrovascular resistance (1, 2). The skull (calvarium), a vascularized bone marrow with highly interconnected vascular channels facilitating the trafficking of immune cells directly to the brain surface (3–5). Yet, a detailed depiction of fluid dynamics in pial as well as calvarial vessels remains remarkably incomplete, mainly due to the lack of quantitative hemodynamic imaging systems.

Past work provided detailed reconstructions of brain vasculature with impressive geometrical precision attainable (6–8). While highly informative, these reconstructions originate from *ex vivo* imaging and thus do not provide functional information. Currently, most hemodynamic imaging techniques exhibit trade-offs in terms of imaging speed, quantitation, and invasiveness. While advances in mesoscale imaging techniques such as laser speckle contrast imaging (LSCI), optical coherence tomography (OCT), and magnetic resonance imaging have enabled monitoring of cerebral blood flow, these techniques suffer from limited spatiotemporal resolution and/or lack of quantitative measurements (9–11). On the other hand, the current state-of-the-art two-photon fluorescence laser scanning microscopy (TPLSM) allows for quantitative blood flow measurements in preselected vessels utilizing line-scanning with maximal detectable velocities limited by the speed of scanning systems (12, 13). Recently developed technology now shifts TPLSM to kilo-Hertz frame rates which comes with some advantages for hemodynamic imaging, however limited to two dimensions (12, 13). TPLSM requires a cranial window preparation, which prohibits concurrent imaging calvarial and cortical vessels. Ultrafast ultrasound localization microscopy captures brain hemodynamics down to the microvascular level. However, imaging the pial vasculature is not possible (14, 15), because the projection of ultrasound echoes in one plane renders hemodynamic measurements valid only for vessels aligned with the axial direction hence the method is suitable only for coronal or sagittal field of views (FOV).

Here, we present a large-scale imaging platform (Pia-FLOW) capable of structural and quantitative hemodynamic imaging of pial and calvarial vascular networks. With this method, we successfully captured the vascular architecture and blood flow dynamics at a spatial resolution of 5.4  $\mu\text{m}$  (full width at half maximum, FWHM) and frame rates up to 1 kHz. Using Pia-FLOW, we provide maps of the pial and calvarial vascular networks across cortex-wide FOVs, which include quantitative information on vessel diameter,

## Significance

The brain and skull harbor intricate vascular systems: 1) The pial arterial network, which is the sole source of blood supply to the neocortex and 2) the calvarial vasculature, residing within the skull and tightly connected to the brain surface. Despite their importance for proper brain functioning, quantitative hemodynamic information of these vascular networks remains scarce. Based on a large-scale fluorescence localization microscope, termed Pia-FLOW, we were able to provide precise hemodynamic maps of the entire pial and calvarial vasculature in mice. Our quantitative mapping covers blood flow velocities, directions, and vascular diameters. Finally, we uncovered how the pial vascular network adapts to ischemic stroke, where blood flow is robustly allocated from main pial arteries to the site of occlusion.

Author contributions: C.G., S.W., D.R., B.W., and M.E.A. designed research; C.G., Q.Z., J.D., Z.C., and M.E.A. performed research; C.G., Q.Z., J.D., Z.C., and L.G. analyzed data; and C.G., B.W., and M.E.A. wrote the paper.

The authors declare no competing interest.

This article is a PNAS Direct Submission.

Copyright © 2024 the Author(s). Published by PNAS. This open access article is distributed under [Creative Commons Attribution-NonCommercial-NoDerivatives License 4.0 \(CC BY-NC-ND\)](https://creativecommons.org/licenses/by-nc-nd/4.0/).

<sup>1</sup>C.G. and Q.Z. contributed equally to this work.

<sup>2</sup>To whom correspondence may be addressed. Email: [bweber@pharma.uzh.ch](mailto:bweber@pharma.uzh.ch) or [mohamad.elamki@usz.ch](mailto:mohamad.elamki@usz.ch).

This article contains supporting information online at <https://www.pnas.org/lookup/suppl/doi:10.1073/pnas.2402624121/-/DCSupplemental>.

Published July 2, 2024.

blood flow velocity and direction. We applied Pia-FLOW to quantify cerebral hemodynamic changes occurring in the pial vascular network after middle cerebral artery occlusion and identified diameter and flow changes in the arterial inflow, pial collaterals, and venous outflow with an accuracy beyond conventional imaging techniques. Pia-FLOW offers different opportunities to investigate the principles of brain fluid dynamics.

## Results

**Pia-FLOW Design and Performance in Terms of Blood Flow Measurements.** The current study presents both an experimental setup and dedicated data processing pipeline for dynamic imaging of brain pial and calvarial vascular networks. A simplified diagram of the Pia-FLOW system is shown in Fig. 1*A*. The system is based on a large-scale microscope equipped with a 473 nm continuous wave (CW) laser as excitation source and a high-speed sCMOS camera, for fluorescence detection of intravenously injected beads (FMOY, orange-yellow fluorescent microspheres, 50  $\mu\text{L}$  of  $2 \times 10^8$  beads/mL) (*SI Appendix*, Fig. S1*A* and Table S1 and Fig. 1*A*) (16). In brief, the laser beam was expanded with a lens pair consisting of a convex lens and an objective to provide widefield illumination. Backscattered fluorescence was then collected with the same objective, focused with a tube lens and recorded by the camera. Through continuous detection of the intravenous injected FMOY fluorescent beads (50  $\mu\text{L}$  volume,  $2 \times 10^8$  beads/mL concentration), flow dynamics within vessels could be retrieved using Pia-FLOW at a frame rate in the range of 400 to 1,000 Hz, enabling blood flow velocity measurements up to 20 mm/s. The size of FMOY beads was quantified with TPLSM (*SI Appendix*, Fig. S1*A*). Additionally, the clearance curve of beads in vivo was measured with Pia-FLOW, revealing a short circulation time (*SI Appendix*, Fig. S1*B*). During this period, negligible capillary stall events, with their incidence being comparable to spontaneous capillary occlusions by red blood cells (RBCs) and neutrophils were observed (17), as confirmed with TPLSM (*SI Appendix*, Fig. S1*C*). We also examined the impact of FMOY beads on innate blood flow by measuring the flow velocities before and after beads injection, where no significant differences in flow velocities were observed (*SI Appendix*, Fig. S1*D*).

Given that TPLSM is the most popular method for in vivo imaging, we imaged the same mouse brains with a  $3 \times 3$  mm cranial window using both TPLSM and Pia-FLOW to compare the spatial resolution and accuracy of velocity estimation. First, we obtained a volumetric image stack of 200  $\mu\text{m}$  using TPLSM covering all pial vessels to generate a maximum intensity projection (MIP) (Fig. 1*B* and *C*). Using Pia-FLOW, we generated high-resolution reconstructions of the pial vascular network with high-quality depictions of the vascular topology down to a 5.4  $\mu\text{m}$  (full width half maximum; FWHM) resolution (Fig. 1*B* and *C*). In the intensity maps, fine details of vascular morphology were evident even in the smallest capillaries (Fig. 1*B* and *C*). We also obtained a similar signal intensity and angiography from TPLSM. Coregistration between Pia-FLOW and TPLSM revealed that both tools resolved the vascular architecture with nearly identical contrast and resolution for vessels with diameters larger than 10  $\mu\text{m}$ . In contrast, we noted an advantage of TPLSM in regard to brain capillaries  $<5$   $\mu\text{m}$  as only limited structural details were discernible in the Pia-FLOW configuration, potentially attributable to the spatial resolution of Pia-FLOW.

With Pia-FLOW, our goal was not only to achieve a robust in vivo mapping of the vascular architecture but also to quantify flow rates and vascular diameters. Toward this goal, we utilized a particle tracking algorithm to extract the motion of fluorescent beads in the blood

circulation. Typically, we performed continuous recording for 60 to 180 s, corresponding to 25,000 to 180,000 frames. Capitalizing on the precise temporal tracking of the sparsely distributed particles, we accurately extracted blood flow velocities and vessel diameters with a large dynamic range (from 0 to 20 mm/s and 5.4  $\mu\text{m}$  to several hundred microns, respectively) (Fig. 1*D* and *E*). Representative time-lapse images of a single particle flowing in a selected vessel are depicted in Fig. 1*E* with a 2D velocity map reconstructed. The parabolic velocity profile across a large vessel is expected (Fig. 1*F*) and is in good agreement with the literature (13, 18). Since the number of particles that appear at each pixel was random, we averaged the flow velocity and direction values of different particles flowing across each pixel accordingly. Superimposing a sequence of images, we obtained high-resolution velocity maps of the entire pial vasculature (Fig. 1*D* and *Movie S1*).

To validate the accuracy of Pia-FLOW in quantifying hemodynamics, we selected vessels with different sizes inside the cranial window and performed TPLSM diameter and velocity line scans along the selected vascular segments. The Pia-FLOW estimates of blood flow speed and diameter at rest, are in reliable agreement with measurements made using TPLSM in the cortex. Scatter-plots and Bland–Altman plots show a good agreement between the two methods over a wide measurement range (Fig. 1*G* and *H*). The feasibility of recording flow velocity by tracking FMOY beads was further validated through the measurements of beads flow alongside blood cells using line scanning with TPLSM, where similar flow velocity values were observed for both targets (*SI Appendix*, Fig. S1*E*). A significant advantage of Pia-FLOW is the ability to perform simultaneous flow measurements across different vessels. A large network of pial vessels can be scanned within 1 to 3 min. An in vivo example of this hemodynamic recording with the resulting blood flow speed and directions is shown in *Movies S1* and *S2*. In contrast, imaging the same vessels with TPLSM took several hours. Overall, these results confirm that Pia-FLOW provides rapid simultaneous structural mapping and accurate hemodynamic quantifications with high spatiotemporal resolution.

**Transcranial Hemodynamic Imaging Using Pia-FLOW.** To apply Pia-FLOW for whole cortex imaging, it is critical to be able to perform recordings not only in mice with implanted cranial windows but also through the intact skull. Toward this goal, we further enlarged the FOV to  $11 \times 11$  mm<sup>2</sup> by using a different camera lens to image the entire brain transcranially. We reconstructed detailed structural maps of the entire pial microvascular network in both intact skull and cranial window implanted mice for comparative analysis (Fig. 2*A–I*). The excellent spatial resolution along the whole brain (Fig. 2*E–H*) enabled us to easily distinguish the three major arteries supplying the cerebrum (anterior, middle, and posterior cerebral arteries, ACA, MCA, and PCA). Furthermore, we compared flow speeds from vessels imaged through a cranial window (Fig. 2*A–D*) to those imaged transcranially (Fig. 2*E–H*). Based on the vessel diameter and flow direction, vessels were divided into three groups: arteries/arterioles, veins/venules, and capillaries. (Fig. 2*I*). We found that the transcranial velocities were in excellent agreement with the values measured through a cranial window (Fig. 2*I* and *SI Appendix*, Fig. S2). It is noteworthy that enlarging the FOV of Pia-FLOW to cover the entire pial network allowed for quantitative blood flow imaging in  $\sim 4,000$  vessel segments at the same time.

In lower-order arterial branches (100 to 200  $\mu\text{m}$ ), the measured blood flow speed was the highest and decreased progressively in higher-order arteries and arterioles (50 to 100  $\mu\text{m}$ ) to reach the lowest rate in pial collaterals (terminal arterial branches)

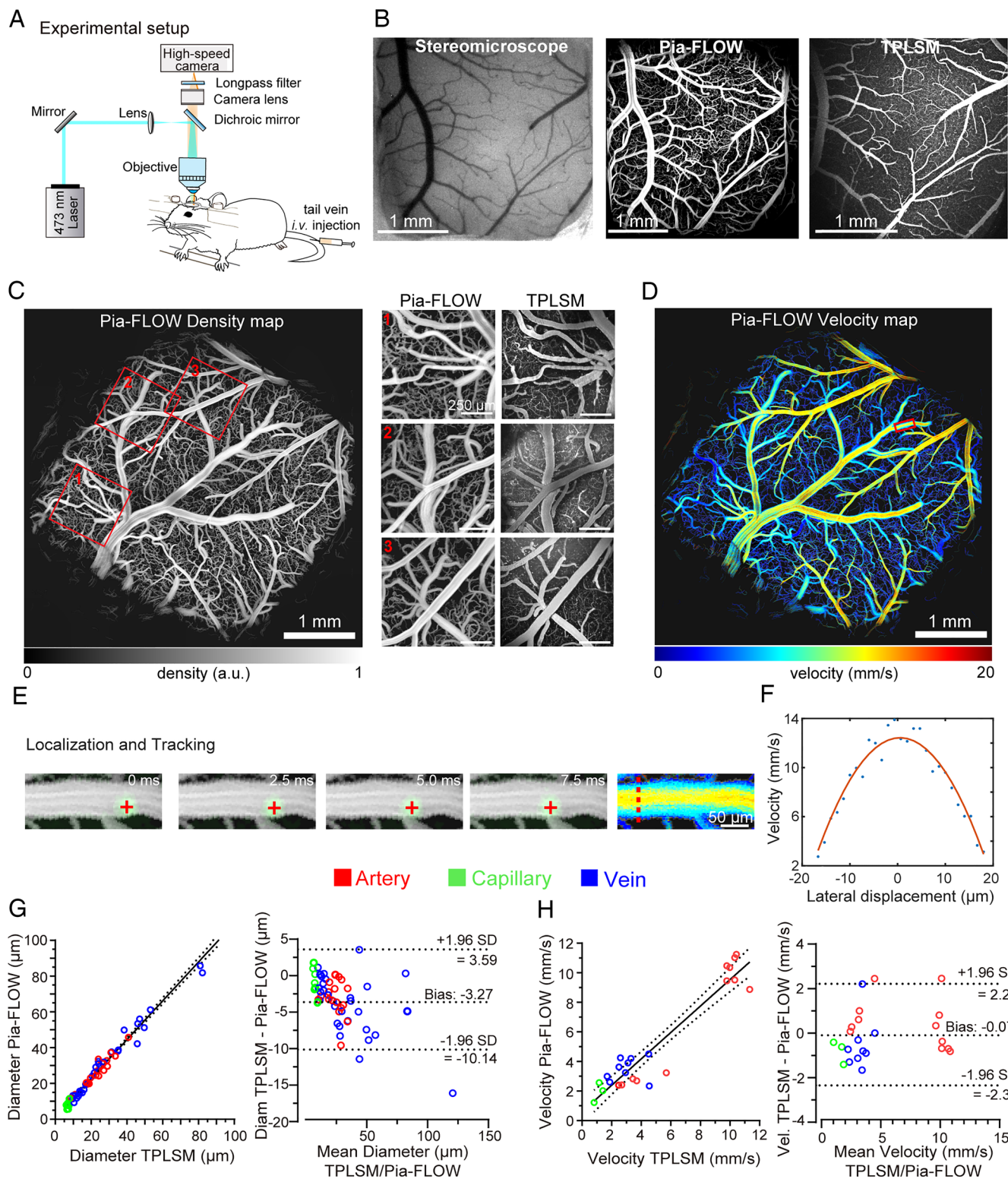


**Fig. 1.** (A) Schematic of Pia-FLOW setup. (B) Stereoscopic, Pia-FLOW, and TPLSM images of the same mouse brain vasculature. (C) Representative intensity map of the mouse brain with a cranial window recorded with Pia-FLOW post fluorescent beads injection. The red squares (1 to 3) indicate zoom-in views to compare the structural map acquired with Pia-FLOW to TPLSM (on the Right). (D) Color-encoded flow velocity map. (E) Time-lapse images of a flowing fluorescence bead in the region of interest (ROI) indicated with a red rectangle in (D). (F) Flow velocity along the red line labeled in (E) plotted as a function of the distance from the vessel center, fitted with a blunted parabolic function. (G) Scatter plot,  $r^2 = 0.98$  (Left) and Bland-Altman plot (Right) of vessel diameters measured with TPLSM and Pia-FLOW, (55 vessels). (H) Scatter plot,  $r^2 = 0.90$  (Left) and Bland-Altman plot (Right) of blood flow velocities measured with TPLSM and Pia-FLOW, (24 vessels). Vessel types are indicated as artery (red), capillary (green), and veins (blue).

(Fig. 2 C and G). Collaterals were easily observable as tortuous segments cross-connecting arterial branches with opposing flow directions: right to left (in orange) and left to right (in blue) (Fig. 2 D and H). Moreover, our data confirm that flow velocity

is higher in arteries/arterioles than size-matched veins/venules (Fig. 2J) which is consistent with previous findings (19–21). Fig. 2K shows the color-encoded flow direction map allowing the differentiation between veins, arteries, and collaterals (Fig. 2L

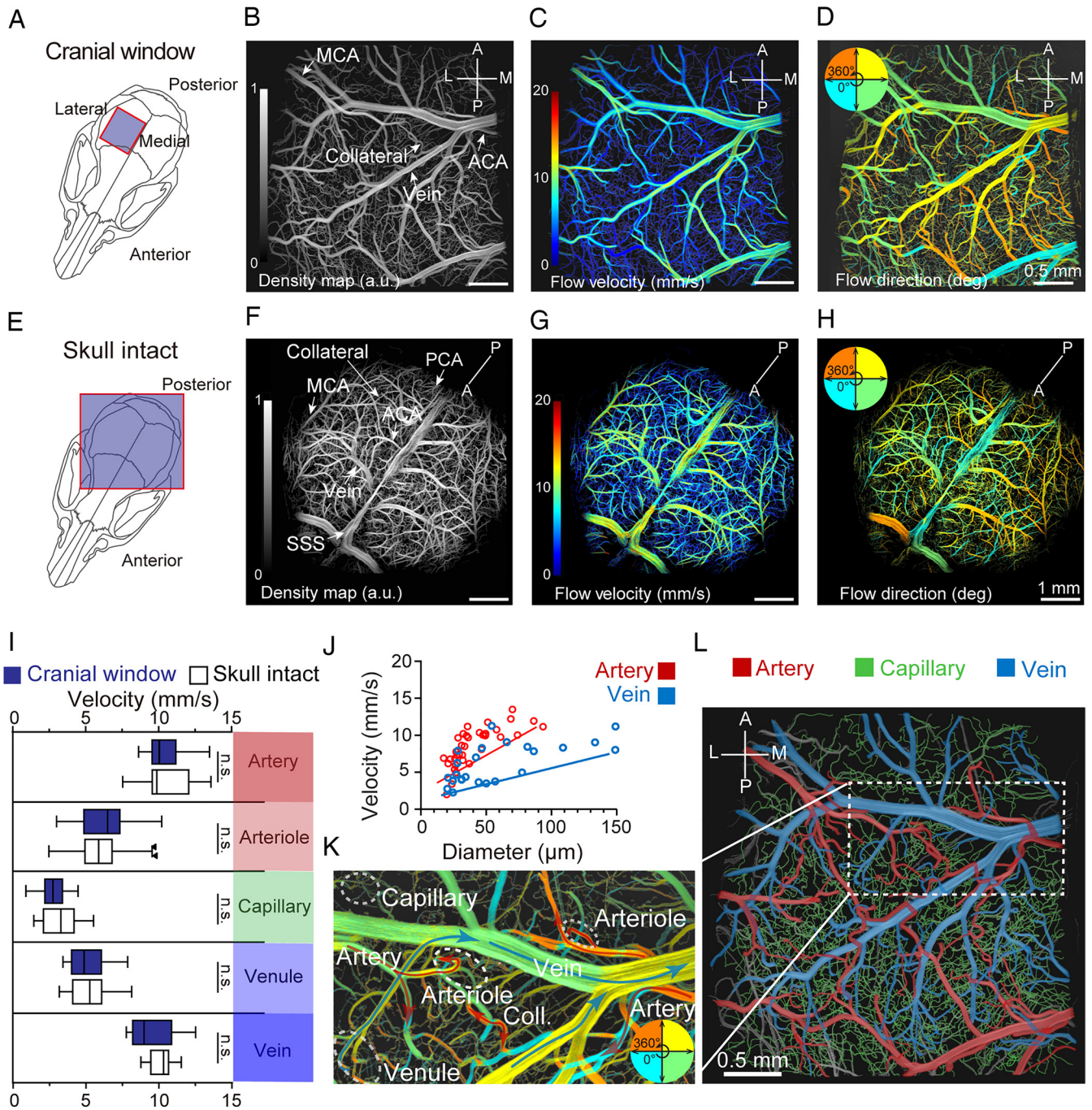


**Fig. 2.** (A) Pia-FLOW measurement of a mouse with a cranial window implanted, showing (B) density map, (C) blood flow velocity, and (D) directionality. The colored cross scale shows flow direction in degrees with different colors: first quarter: cyan; second quarter: Green; third quarter: yellow; fourth quarter: orange. (E) Pia-FLOW measurement performed transcranially, showing (F) density map, (G) blood flow velocity, and (H) directionality. (I) Quantification of blood flow velocities in arteries, arterioles, capillaries, venules, and veins comparing cranial window (dark blue) with transcranial (white) Pia-FLOW measurements.  $N = 3$  mice for each group. Unpaired  $t$  tests, n.s. = not significant. (J) Scatter-plot of vessel diameter versus velocity for veins,  $r^2 = 0.43$  (blue) and arteries,  $r^2 = 0.55$  (red). (K) Indication of flow direction of a zoom-in region (indicated by dashed white square in (L) Segmentation of arteries (red), veins (blue), and capillaries (green) based on flow direction in (D).

and [Movie S2](#)). Our Pia-FLOW microscope can also be used for tracking sparsely labeled RBCs. To demonstrate the capability of Pia-FLOW in brain-wide hemodynamic imaging by tracking fluorescently labeled RBCs, we performed *ex vivo* labeling of RBCs using a fluorescent dye named DiD, followed by *i.v.* injection to mice. A flow velocity map could be then rendered with Pia-FLOW in the same way as beads ([SI Appendix, Fig. S1 F and G](#)), although the original widefield images exhibited a much lower signal-to-noise ratio (SNR) compared to those obtained from FMOY beads.

#### Hemodynamic Imaging of the Calvarium Using Pia-FLOW.

Next, we evaluated the ability of our method to measure blood flow dynamics in the skull. The skull bone marrow is considered as the immune cell reservoir for the brain and calvarial vessels act as gates for the blood exchange between skull marrow and brain. To date, many fundamental questions regarding the vascular architecture and blood flow in the calvarium remain unresolved. The transcranial imaging capabilities of Pia-FLOW enabled us to conduct hemodynamic imaging in calvarial vessels, beyond the reach of conventional angiographic methods such as TPLSM ([Fig. 3 A–C](#)).

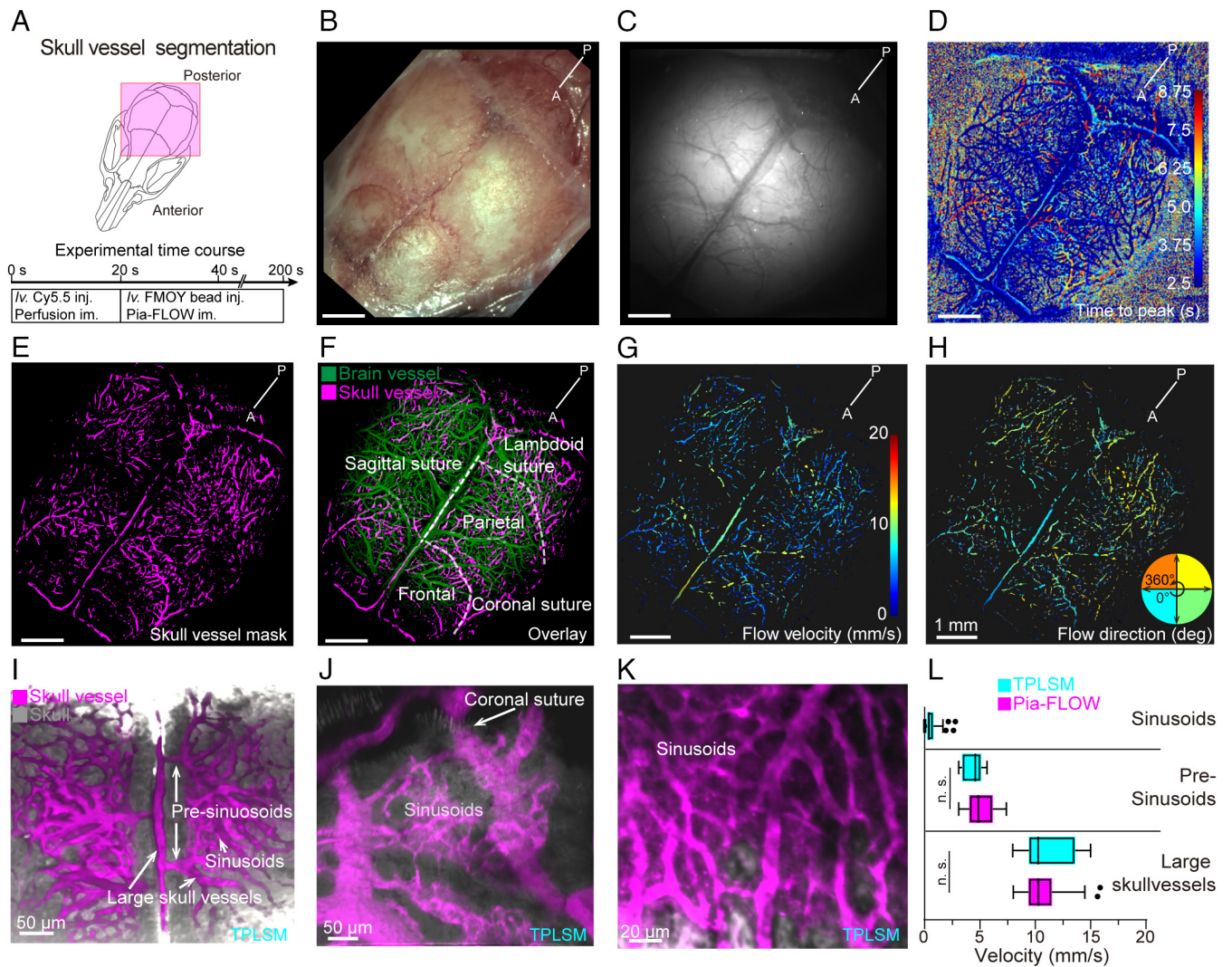


**Fig. 3.** (A) Schematic of the skull vessel area imaged. Below, experimental time course for skull vessel imaging. (B) Exposed skull surface. (C) Skull illuminated with wide-field microscopy. (D) Time to peak (s) map of vessel perfusion upon *i.v.* dye injection. (E) Segmented skull vessel mask, based on time to peak map. (F) Overlay of skull vessel (magenta) onto pial vessels of the brain (green). Dashed white lines outline the skull plates and sutures. (G) Flow velocity and (H) flow direction map of skull vessels. (I–K) TPLSM images of skull vasculature indicating structure of large skull vessels, presinusoids, and sinusoids. (L) Quantification of the skull vessel blood flow velocity comparing Pia-FLOW and TPLSM.  $N = 4$  mice. Unpaired Mann–Whitney  $U$  test, n.s. = not significant.

Using Pia-FLOW, we constructed the first velocity map of the murine calvarial vessels by the intravenous injection of Cy5.5 fluorescent dye followed by fluorescent beads. The time-to-peak (TTP) map generated from the dye perfusion process (Fig. 3D) served as a benchmark for segmenting calvarial vessels from pial vessels on the structural map reconstructed from Pia-FLOW (Fig. 3E–H). For comparison, we also imaged skull vessels with TPLSM and found that flow velocities in large skull vessels and presinusoids correspond well with Pia-FLOW measurements (Fig. 3I–L). However, Pia-FLOW was not able to capture sinusoids, due to their small size, and irregular, low flow. Overall, our data demonstrate the capability of Pia-FLOW to perform simultaneous pial and calvarial hemodynamic imaging at single-vessel resolution.

**Measuring the Response of the Pial Vasculature to MCA Occlusion Using Pia-FLOW.** To further extend our technique to cerebrovascular research, we used Pia-FLOW to assess brain hemodynamics in the “thrombin” model of stroke in mice (Fig. 4A). Here, we compared Pia-FLOW with LSCI, which is another widefield imaging technology commonly used in stroke research. We collected datasets from three mice, and each mouse was imaged with both modalities before and after stroke. In terms of spatial

resolution, our technology demonstrated a clear advantage over LSCI by identifying some well-resolved vessel subtypes that remain undetected in the LSCI image (Fig. 4B and C). This difference became even more evident after stroke where the entire stroke area was blurred out, and LSCI failed to discern details on a single vessel level (Fig. 4C). To quantify flow changes in specific vessels, we used Pia-FLOW baseline images as reference and merged it with the corresponding LSCI image to select the same vessel segments for comparative analysis. We selected representative branches from arteries, arterioles, collaterals, venules and veins within the ischemic area. Pia-FLOW showed a reduction of blood flow in the highly interconnected arterial branches of the occluded MCA. The largest flow decreases ( $\sim 70\%$ ) were observed in high-order arteries that were within a few branches downstream from the occluded segment (Fig. 4E). Lower-order (or more downstream) MCA branches (arterioles and penetrating arterioles) showed smaller flow rate reductions (Fig. 4E). The extent of affected vessels within the whole brain after stroke is represented in Fig. 4F and *SI Appendix, Fig. S3 A and B*. Importantly, Pia-FLOW revealed that only collaterals showed significant increases in flow speed to redistribute blood supply to the affected arterial territory while the flow in ACA segments remained unchanged. These data are in

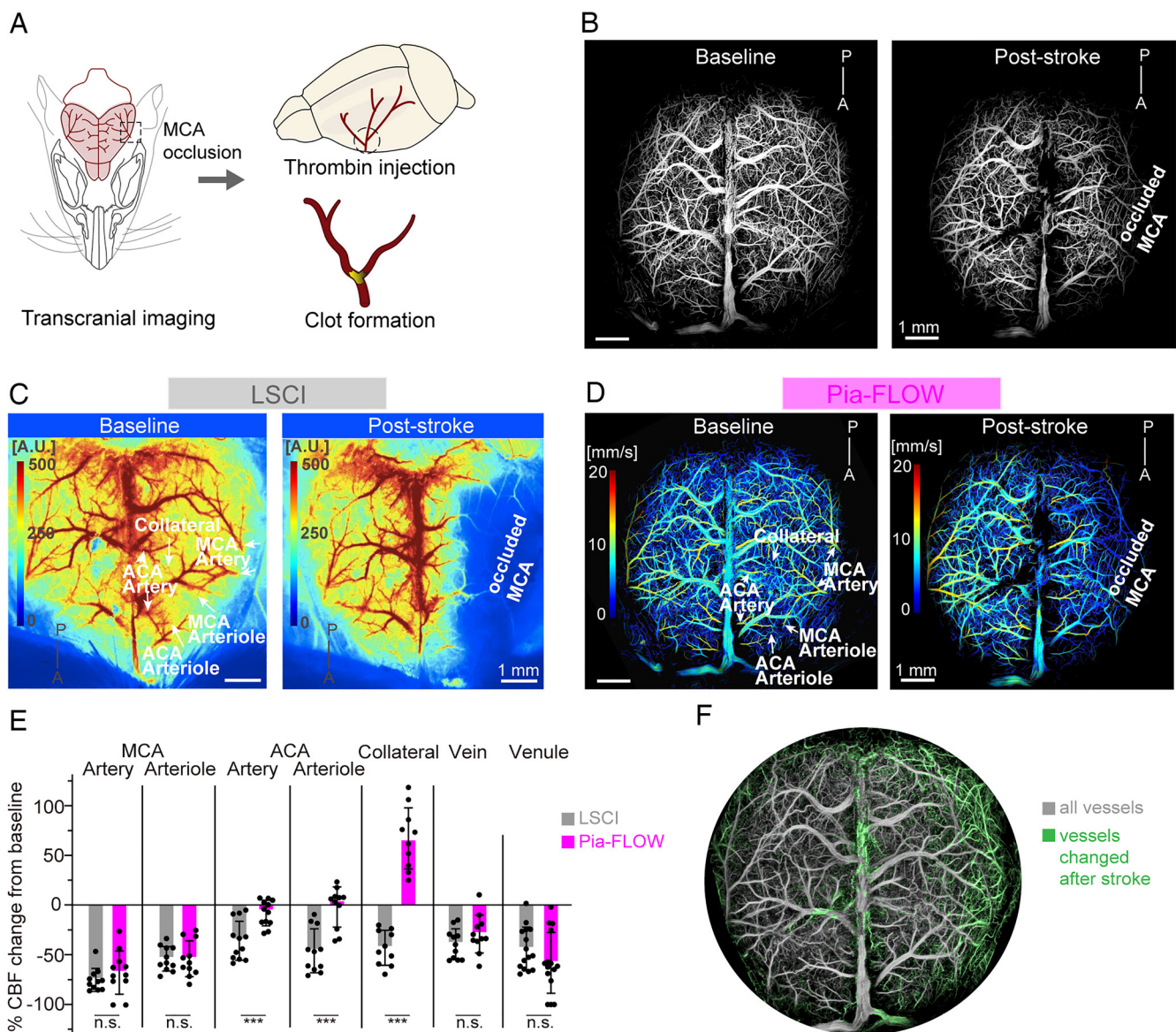


**Fig. 4.** (A) Schematic of the stroke model. (B) Density images of a mouse at baseline and poststroke. (C) Images of the same mouse brain acquired by LSCI and (D) Pia-FLOW at baseline and poststroke showing perfusion or blood flow velocities. (E) Quantification of the change of blood flow in percentage of baseline.  $N = 3$ , n.s. = not significant, \*\*\* $P < 0.001$ . (F) Overlaid image of a mouse brain acquired by Pia-FLOW showing vessel coverage pre- and poststroke.

line with previous TPLSM studies that discovered the engagement of collateral to reroute blood flow in stroke conditions (22, 23). In contrast to Pia-FLOW, LSCI was not sensitive enough to specifically detect the flow increase in collaterals but surprisingly showed flow reductions in both pial collaterals and ACA segments (Fig. 4E). Taken together, our results indicate that Pia-FLOW outperforms LSCI in terms of spatial resolution and accuracy in hemodynamic recordings.

**The Pial Vasculature Responds As a Connectome after MCA Occlusion.** Next, we took advantage of Pia-FLOW to investigate how each individual vessel in the pial network adapts in response to an arterial occlusion. Such experiments were previously difficult due to the need of simultaneous and quantitative measurements from the pial vasculature. For example, using TPLSM for this purpose takes several hours which renders capturing acute and transient effects impossible.

As pial collaterals are a natural bypass that can redistribute blood flow to ischemic regions, we primarily focused on these vascular segments. Previous work of us and others showed that

after arterial occlusion, collaterals dilate and change flow direction (22, 23). However, it is unknown whether all pial collaterals change flow direction after stroke and to what extent collaterals are capable of compensating blood flow in the affected region. Fig. 5 A and B shows a specific vascular network before and after MCA occlusion. This network includes high- and low-order arterial segments from MCA, ACA, and pial collaterals. First, we observed that under baseline conditions, collaterals show a preference in blood flow direction (some from MCA to ACA and others reversibly; Fig. 5 and *SI Appendix, Fig. S3*). The flow direction preference was defined by the higher flow gradient between MCA and ACA. Further, we observed that after MCA occlusion, collaterals redistribute blood from ACA to MCA which is in line with previous studies showing the role of collaterals in rerouting blood flow to the ischemic area (22–24).

Interestingly, changes in blood flow direction occurred only in collaterals flowing originally from MCA to ACA. Altogether, our data show precisely how blood flow is rerouted from ACA via collaterals to MCA in order to compensate the flow reduction in ischemic stroke regions (*SI Appendix, Fig. S3* and *Movies S3* and *S4*).

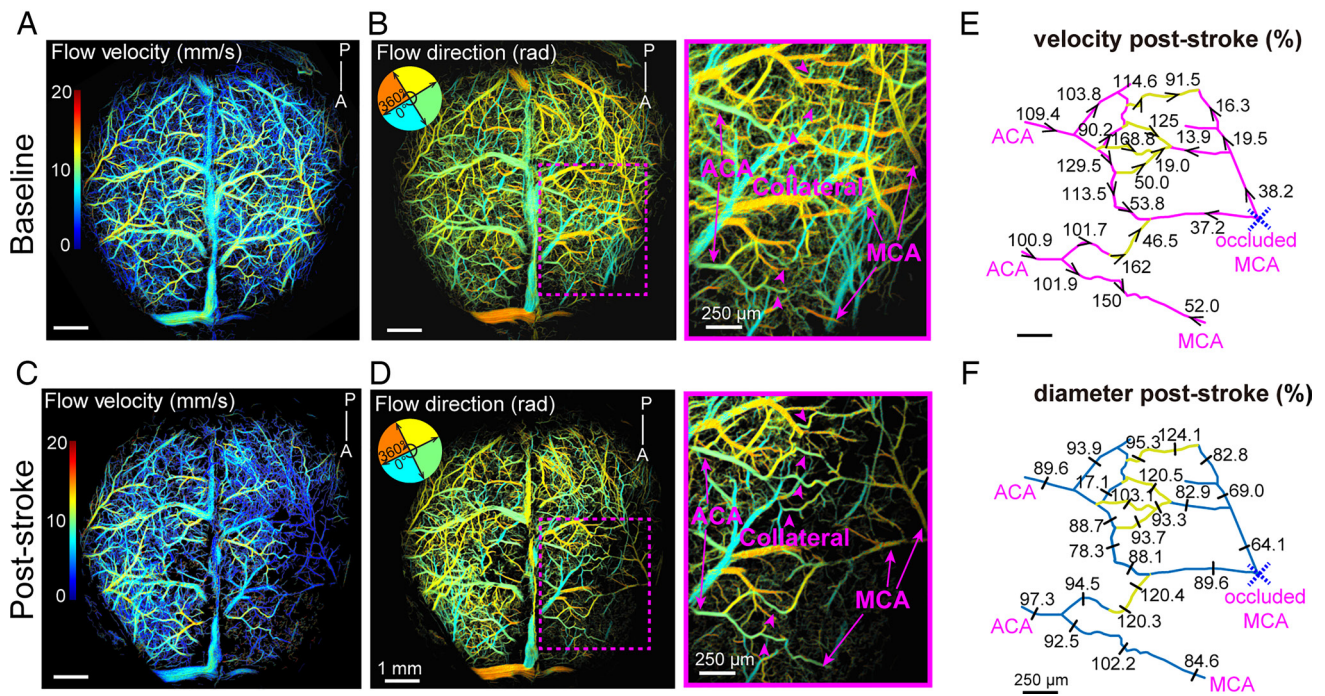


**Fig. 5.** (A–D) Flow velocity and direction maps at baseline and poststroke. The zoom-in on the right (indicated by the dashed magenta square) highlights the position of collaterals (arrowheads). (E and F) Extracted arterial network. Values indicate (E) velocities and (F) diameters measured at indicated position with the arrowhead indicating the flow direction and shown as percent change compared to baseline value. Vessel segments with inverted flow direction poststroke are indicated in yellow.

## Discussion

Here, we presented Pia-FLOW, a mesoscale localization microscopy technique for structural and functional imaging of the pial and calvarial vasculature. We emphasize that Pia-FLOW concurrently achieves the following key benchmarks: 1) cortex-wide FOV, 2) transcranial imaging capability, 3) fast sampling rate (up to 1 kHz), 4) single-vessel resolution, and 5) quantitative measurements of flow velocity and vessel diameter.

We achieved a cortex-wide FOV not reachable with most of the available quantitative blood flow imaging tools. For example, conventional TPLSM is limited to sampling only a portion of the tissue accessible via cranial windows, unless a tiling strategy is used (25). To the best of our knowledge, no technology today comes close to being able to simultaneously track the entire pial vasculature at single-vessel resolution. Quantitative assessments of blood flow in the pial vasculature remained a major challenge impeding investigations of brain function and cerebrovascular diseases at large scale (26). Conventional widefield methods, such as LSCI, are limited with respect to their spatial resolution and only provide relative velocity measurements (27). Another key advantage of Pia-FLOW is its ability to perform quantitative and simultaneous blood flow measurements. TPLSM allows quantitative calculation of flow speed and diameters, however, this requires individual 1D line scans on each vessel making mapping the whole vasculature almost impossible. Although this problem could be overcome by using TPLSM Bessel beam, however, the maximum detectable velocity is around 3 mm/s constrained by the 2D frame rate of 99 Hz (28). Our widefield localization technique allows for the direct quantification of blood flow velocity (up to 20 mm/s) and diameters in hundreds of vessels synchronously. This can be particularly useful in cases where multiple vessels need to be measured synchronously in the whole brain vascular connectome. Outcomes from our work will supply the field with practical hemodynamic maps of the brain vasculature. Pia-FLOW now allows systematic

hemodynamic studies that will enhance our understanding of the pathophysiology of cerebrovascular disease.

Pia-FLOW is an easy and straightforward method that can be combined with existing widefield imaging systems used for fluorescence calcium imaging for neuronal activity. By incorporating these features, our microscope could be extended to synchronously measure blood flow and neuronal activity to study brain function in physiology and disease, such as neurovascular coupling and spreading depolarization.

Moreover, Pia-FLOW holds another key advantage because it allows imaging through the skull. This keeps the physiological environment of the brain intact. Previous studies showed that excision of calvarial bone to implement a cranial window may inadvertently remove parts of the dura (29) and also perturbate brain and vascular functions (30, 31). Although imaging through mechanically thinned skull bone reduces these problems (30), this may also cause trauma to trigeminal nerve terminals in the calvarium and inflammation of the dura by the axon reflex (32). Our study also demonstrates that Pia-FLOW can be used for noninvasive-transcranial imaging of the calvarial vasculature and provides topological, morphological, and hemodynamic information. This becomes increasingly important because of a growing interest in the skull marrow as a neuroimmunological niche (33). In fact, there is recent evidence that skull marrow is a myeloid cell reservoir for the central nervous system parenchyma (4). The skull vasculature provides signals for the maintenance and proliferation of hematopoietic stem and progenitor cells in the bone marrow (4). Previous work using optoacoustic and ultrasound microscopy allowed imaging of the calvarial morphology but hemodynamic information was hard to achieve with this method (34). Thus, Pia-FLOW is a promising tool that can be used to further study the vasculature in the skull marrow microenvironment to better understand how calvarial and pial vascular networks interact to regulate immune trafficking with the brain. However, flow in small sinusoidal vessels is very low and irregular and thus difficult to capture with Pia-FLOW or TPLSM.

Another limitation is that we could not extract quantitative maps from the dura vessels; however, further studies with vessel-specific markers and manipulation of arterial supply routes may enable such investigations.

Using our method for proof-of-principle synchronous recording of the entire pial vasculature, we showed that after an arterial obstruction, the flow and diameter changes affect almost every pial vessel within the vascular network. More precisely, we took advantage of the ability of Pia-FLOW to perform cortex-wide simultaneous imaging and provided detailed insight into the spatial coupling of pial collaterals to the occluded and neighboring arterial branches. Our data showed that the whole brain vascular network react as a connectome where pial vessels redistribute blood to the ischemic territory via collaterals. Of note, such measurements would be incremental to understand recanalization/perfusion and No-Reflow in stroke (35).

Finally, owing to the simple optical design, Pia-FLOW offers the potential to install an additional fluorescence channel for labeling other blood components such as leukocytes, red blood cells, or plasma. We anticipate further important applications of Pia-FLOW, such as *in vivo* imaging of leukocyte trafficking in pial vessels, immune cells transition from the calvarium to the brain, and *in vivo* imaging of tumor metastasis.

Overall, Pia-FLOW achieves transcranial recordings of the pial and calvarial hemodynamics with high spatial and temporal resolution. Its ability to simultaneously measure blood flow in multiple vessels makes it a valuable tool to understand the control of blood flow in the brain. We expect Pia-FLOW to become a widely used tool to investigate the brain and calvarial vascular biology and to find widespread applications in neuroimmunology and neurobiology.

## Materials and Methods

**Ethics and Animals.** Experiments were conformed to the guidelines of the Swiss Animal Protection Law, Veterinary Office, Canton of Zurich (Act of Animal Protection December 16, 2005, and Animal Protection Ordinance April 23, 2008, animal welfare assurance number ZH224/15 and ZH165/19). Experiments were performed on both male and female C57Bl6/J mice (Charles Rivers, no.028), 6 to 12 wk of age, weighing between 20 and 30 g. The mice were housed under standard conditions including free access to water and food as well as an inverted 12-h light/dark cycle.

**Anesthesia.** For headpost and cranial window implantation, animals were injected intraperitoneally with a triple mixture of fentanyl (0.05 mg/kg body weight; Sintenyl, Sintetica), midazolam (5 mg/kg body weight; Dormicum, Roche), and medetomidine (0.5 mg/kg body weight; Domitor, Orion Pharmaceuticals). The face mask delivers 100% oxygen at a rate of 300 mL/min. For stroke induction, Pia-FLOW, TPLSM, and LSCI imaging, mice received the same triple anesthesia mixture intraperitoneally. During all procedures, the animals' core temperature was maintained at 37 °C using a thermostatic blanket heating system (Harvard Instruments).

**Thrombin Stroke Model.** To induce ischemic stroke, we used the thrombin model to induce stroke as previously described (36, 37). Briefly, a glass pipette was inserted into the lumen of the MCA, and 1  $\mu$ L of thrombin (1 UI; HCT-0020, Haematologic Technologies Inc.) was injected to induce *in situ* clot formation (Fig. 3). To enhance the clot stability, the pipette was removed 10 min later.

**Scalp Removal and Cranial Window Preparation.** A 4  $\times$  4 mm craniotomy was drilled above the somatosensory cortex using a dental drill (Bien-Air). A square coverslip (3  $\times$  3 mm, UQG Optics) was then placed on the exposed dura mater and fixed to the skull with dental cement (38). After cranial window implantation, mice were allowed to recover for 2 wk prior to TPLSM imaging. For transcranial imaging, the skull of the mouse was kept intact while the scalp was removed to reduce light scattering. To minimize bleeding, hemostatic sponges (Gelfoam<sup>®</sup>, Pfizer Pharmaceutical) were used together with a topical application of adrenaline.

**Laser Speckle Contrast Imaging.** Cortical perfusion was monitored before and after ischemia using Laser speckle imaging monitor (FLPI, Moor Instruments, UK). The laser speckle images are generated with arbitrary units in a 32-color palette by MoorFLPI software.

**Two-Photon Imaging.** Two-photon imaging was performed using a custom-built TPLSM (39) with a tunable pulsed laser (Chameleon Discovery TPC, Coherent Inc.) equipped with a 25 $\times$  water immersion objective (W-Plan-Apochromat 25 $\times$ /1.0 NA, Olympus, Japan). During measurements, the animals were head-fixed and kept under anesthesia as described above. To visualize the vasculature, Cascade blue dextran (5% w/v, 10,000 kDa MW, 100  $\mu$ L, D-1976, Life Technologies, USA) was injected intravenously 10 min before imaging and was excited at 820 nm. To validate the flow behavior of FMOY beads, 50  $\mu$ L of fluorescent beads (1 to 5  $\mu$ m, FMOY, Cospheric) in saline were injected via tail vein at a concentration of  $2 \times 10^8$  beads/mL. Line scan and z stacks were performed before and after beads injection to compare vessel segments and their respective flow speeds (SI Appendix, Fig. S1). Emission was detected with GaAsP photomultiplier modules (Hamamatsu Photonics, Japan) fitted with a 475/64 nm bandpass filter and separated by 506 nm dichroic mirror (BrightLine; Semrock, USA). The microscope was controlled by a customized version of ScanImage [r3.8.1; Janelia Research Campus (40)]. Line scans were processed with a custom-designed image processing tool box for MATLAB [Cellular and Hemodynamic Image Processing Suite (41); R2014b; MathWorks]. Vessel diameters were calculated at full-width-at-half-maximum (FWHM) from a Gaussian-fitted intensity profile drawn perpendicular to the vessel axis and with the "vessel diameter" plugin in ImageJ. Blood flow was determined with the Radon algorithm (42).

**Pia-FLOW Imaging.** A 473 nm continuous wave (CW) laser (FPYL-473-1000-LED, Frankfurt Laser Company, Germany) beam was expanded with a convex lens (LA4306, Thorlabs, USA) and an objective (CLS-SL, EFL = 70 mm, Thorlabs, USA) to provide epi-illumination of the sample. Then, 50  $\mu$ L of fluorescent beads (1 to 5  $\mu$ m, FMOY, Cospheric, USA) in saline were injected via tail vein at a concentration of  $2 \times 10^8$  beads/mL. The concentration injected to different mice was adjusted based on their body weight and the corresponding total blood volume. Backscattered fluorescence was then collected with the same objective, focused with a tube lens (AF micro-Nikkor 105 mm, Nikon, Japan), and detected by a high-speed camera (pco.dimax S1, PCO AG, Germany). A longpass filter (FGL515, Thorlabs, USA) was inserted between the tube lens and camera to filter out the reflected excitation light. The system's magnification was reduced to 1 for transcranial measurements to achieve an enlarged FOV, by using a different camera lens (AF micro-Nikkor 60 $\times$  mm, Nikon, Japan).

**Skull Vessel Imaging.** For skull vessel segmentation, modifications were made to the Pia-FLOW setup to accommodate different fluorescence contrast agents. The laser source was switched to a 660 nm CW laser (gem 660, Laser Quantum, USA). Both the dichroic mirror (Di03-R660-t1-25 $\times$ 36, Semrock, USA) and longpass filter (LP02-671RU-25, Semrock, USA) were changed accordingly, while other components remained unchanged. Widefield recording was conducted following the intravenous injection of 50  $\mu$ L 1 mg/ml Cy5.5 dye (Sulfo-Cyanine5.5 carboxylic acid, 47390, Lumiprobe GmbH, Germany) at a 40 Hz frame rate over a duration of 20 s. For data processing, the image stack was initially denoised by subtracting a preinjection background, followed by Frangi filtering to enhance image contrast. Leveraging the high frame rate, the TTP value for each pixel on the image was determined at the time point when the fluorescence signal reached the peak, rendering a TTP map (Fig. 3D). Due to differences in perfusion time between cerebral and skull vessels (43), skull vessels were segmented by applying a threshold of 3.5 s to the TTP map. The generated skull vessel mask was coregistered to the high-resolution Pia-FLOW image to produce the final skull vessel map using "cpselect" and "fitgeotrans" functions in MATLAB (R2020b, MathWorks, USA).

For TPLSM imaging of skull vessels, the skull was exposed and kept wet with a 1:1 mix of Ringer and ultrasound gel and was covered with a glass coverslip. Blood plasma was stained with cascade blue dextran via *i.v.* tail vein injection.

**Pia-FLOW Image Reconstruction and Processing.** To generate a high-resolution density, flow velocity, and direction maps, the recorded widefield image stack was first denoised by subtracting a moving background calculated from the mean intensity of adjacent images to remove the static background stemming from the autofluorescence and dark noise of the camera. Subpixel

localization was performed by extracting the centroid of bright spots detected using an adaptive threshold. Subsequently, the flowing fluorescent beads were tracked by identifying the same particle in different frames with simpletracker algorithm (simpletracker.m. GitHub <https://github.com/tinevez/simpletracker>, 2019), with no gap gilling and maximum linking distance corresponding to a velocity of 20 mm/s. Functional parameters, such as flow velocity and direction, were calculated with the given frame rate and relative displacement of the same particle in consecutive frames. The intensity map was generated by superimposing the trajectories of beads. Similarly, flow velocity and direction maps were computed by averaging the velocities of all particles flowing through the same pixel. All the image reconstruction and processing were performed with custom code in MATLAB (MathWorks, MATLAB R2020b, USA).

**Quantification and Statistical Analysis.** Parametric statistics were used only if the data in all groups in the comparison were normally distributed. Statistical analysis was performed using the GraphPad Prism (version 8.0; GraphPad Software La Jolla, CA, USA). All statistical tests and group size (n) are indicated in

1. P. Blinder, A. Y. Shih, C. Rafie, D. Kleinfeld, Topological basis for the robust distribution of blood to rodent neocortex. *Proc. Natl. Acad. Sci. U.S.A.* **107**, 12670–12675 (2010).
2. P. Blinder *et al.*, The cortical angiome: an interconnected vascular network with noncolumnar patterns of blood flow. *Nat. Neurosci.* **16**, 889–897 (2013).
3. F. Herisson *et al.*, Direct vascular channels connect skull bone marrow and the brain surface enabling myeloid cell migration. *Nat. Neurosci.* **21**, 1209–1217 (2018).
4. A. Cugurra *et al.*, Skull and vertebral bone marrow are myeloid cell reservoirs for the meninges and CNS parenchyma. *Science* **373**, eab7844 (2021).
5. J. A. Mazzitelli *et al.*, Cerebrospinal fluid regulates skull bone marrow niches via direct access through dural channels. *Nat. Neurosci.* **25**, 555–560 (2022).
6. M. I. Todorov *et al.*, Machine learning analysis of whole mouse brain vasculature. *Nat. Methods* **17**, 442–449 (2020).
7. F. F. Voigt *et al.*, The mesoSPIM initiative: Open-source light-sheet microscopes for imaging cleared tissue. *Nat. Methods* **16**, 1105–1108 (2019).
8. C. Kirst *et al.*, Mapping the fine-scale organization and plasticity of the brain vasculature. *Cell* **180**, 780–795.e725 (2020).
9. S. A. Boppart *et al.*, Noninvasive assessment of the developing Xenopus cardiovascular system using optical coherence tomography. *Proc. Natl. Acad. Sci. U.S.A.* **94**, 4256–4261 (1997).
10. S. Ogawa *et al.*, Intrinsic signal changes accompanying sensory stimulation: Functional brain mapping with magnetic resonance imaging. *Proc. Natl. Acad. Sci. U.S.A.* **89**, 5951–5955 (1992).
11. C. Demene *et al.*, Transcranial ultrafast ultrasound localization microscopy of brain vasculature in patients. *Nat. Biomed. Eng.* **5**, 219–228 (2021).
12. B. Weber, F. Schmid, A FACED lift for cerebral blood flow imaging. *Proc. Natl. Acad. Sci. U.S.A.* **119**, e2207474119 (2022).
13. G. Meng *et al.*, Ultrafast two-photon fluorescence imaging of cerebral blood circulation in the mouse brain in vivo. *Proc. Natl. Acad. Sci. U.S.A.* **119**, e2117346119 (2022).
14. C. Errico *et al.*, Ultrafast ultrasound localization microscopy for deep super-resolution vascular imaging. *Nature* **527**, 499–502 (2015).
15. N. Renaudin *et al.*, Functional ultrasound localization microscopy reveals brain-wide neurovascular activity on a microscopic scale. *Nat. Methods* **19**, 1004–1012 (2022).
16. Z. Chen, Q. Zhou, J. Robin, D. Razansky, Widefield fluorescence localization microscopy for transcranial imaging of cortical perfusion with capillary resolution. *Opt. Lett.* **45**, 3470–3473 (2020).
17. J. C. Cruz Hernandez *et al.*, Neutrophil adhesion in brain capillaries reduces cortical blood flow and impairs memory function in Alzheimer's disease mouse models. *Nat. Neurosci.* **22**, 413–420 (2019).
18. T. Zhang *et al.*, Kilohertz two-photon brain imaging in awake mice. *Nat. Methods* **16**, 1119–1122 (2019).
19. Q. Pian *et al.*, Cortical microvascular blood flow velocity mapping by combining dynamic light scattering optical coherence tomography and two-photon microscopy. *J. Biomed. Opt.* **28**, 076003 (2023).
20. Z. J. Taylor *et al.*, Microvascular basis for growth of small infarcts following occlusion of single penetrating arterioles in mouse cortex. *J. Cereb. Blood Flow Metab.* **36**, 1357–1373 (2016).
21. S. J. Ahn *et al.*, Label-free assessment of hemodynamics in individual cortical brain vessels using third harmonic generation microscopy. *Biomed. Opt. Express* **11**, 2665–2678 (2020).
22. N. F. Binder *et al.*, Leptomeningeal collaterals regulate reperfusion in ischemic stroke and rescue the brain from futile recanalization. *Neuron* **112**, 1456–1472.e1456 (2024).

the figure legends. Results were expressed either as mean  $\pm$  SD). Significance ( $P < 0.05$ ) between two groups was calculated using unpaired Student's *t* test or paired *t* test for normally distributed data or with the Mann-Whitney *U* test for data with nonnormal distribution.

**Data, Materials, and Software Availability.** All study data are included in the article and/or supporting information.

**ACKNOWLEDGMENTS.** We acknowledge the grant support from the Swiss heart foundation, the Swiss NSF: 310030\_192757, US NIH (UF1-NS107680), Innosuisse–Swiss Innovation Agency (51767.1 IP-LS) and the UZH CRPP stroke.

Author affiliations: <sup>1</sup>Institute of Pharmacology and Toxicology, University of Zurich, Zurich 8057, Switzerland; <sup>2</sup>Neuroscience Center Zurich, University of Zurich and ETH Zurich, Zurich 8057, Switzerland; <sup>3</sup>Institute for Biomedical Engineering, Department of Information Technology and Electrical Engineering, ETH Zurich, Zurich 8092, Switzerland; and <sup>4</sup>Department of Neurology, University Hospital and University of Zurich, Zurich 8091, Switzerland

23. J. Ma, Y. Ma, A. Shuaib, I. R. Winship, Impaired collateral flow in pial arterioles of aged rats during ischemic stroke. *Transl. Stroke Res.* **11**, 243–253 (2020).
24. H. Zhang, P. Prabhakar, R. Sealock, J. E. Faber, Wide genetic variation in the native pial collateral circulation is a major determinant of variation in severity of stroke. *J. Cereb. Blood Flow Metab.* **30**, 923–934 (2010).
25. A. Y. Shih *et al.*, Two-photon microscopy as a tool to study blood flow and neurovascular coupling in the rodent brain. *J. Cereb. Blood Flow Metab.* **32**, 1277–1309 (2012).
26. S. W. Hetts *et al.*, Pial artery supply as an anatomic risk factor for ischemic stroke in the treatment of intracranial dural arteriovenous fistulas. *AJNR Am. J. Neuroradiol.* **38**, 2315–2320 (2017).
27. N. F. Binder *et al.*, Vascular response to spreading depolarization predicts stroke outcome. *Stroke* **53**, 1386–1395 (2022).
28. J. L. Fan *et al.*, High-speed volumetric two-photon fluorescence imaging of neurovascular dynamics. *Nat. Commun.* **11**, 6020 (2020).
29. M. E. Walker-Caulfield, J. K. Hatfield, M. A. Brown, Dynamic changes in meningeal inflammation correspond to clinical exacerbations in a murine model of relapsing-remitting multiple sclerosis. *J. Neuroimmunol.* **278**, 112–122 (2015).
30. H. T. Xu, F. Pan, G. Yang, W. B. Gan, Choice of cranial window type for in vivo imaging affects dendritic spine turnover in the cortex. *Nat. Neurosci.* **10**, 549–551 (2007).
31. S. P. Olesen, Leakiness of rat brain microvessels to fluorescent probes following craniotomy. *Acta Physiol. Scand.* **130**, 63–68 (1987).
32. B. Kosaras, M. Jakubowski, V. Kainz, R. Burstein, Sensory innervation of the calvarial bones of the mouse. *J. Comp. Neurol.* **515**, 331–348 (2009).
33. J. A. Mazzitelli *et al.*, Skull bone marrow channels as immune gateways to the central nervous system. *Nat. Neurosci.* **26**, 2052–2062 (2023).
34. H. Estrada *et al.*, Intravital optoacoustic and ultrasound bio-microscopy reveal radiation-inhibited skull angiogenesis. *Bone* **133**, 115251 (2020).
35. M. E. Amki, S. Wegener, Reperfusion failure despite recanalization in stroke: New translational evidence. *Clin. Transl. Neurosci.* **5**, 2514183X211007137 (2021).
36. M. El Amki *et al.*, Neutrophils obstructing brain capillaries are a major cause of no-reflow in ischemic stroke. *Cell Rep.* **33**, 108260 (2020).
37. M. El Amki *et al.*, Experimental modeling of recombinant tissue plasminogen activator effects after ischemic stroke. *Exp. Neurol.* **238**, 138–144 (2012).
38. A. Holtmaat *et al.*, Long-term, high-resolution imaging in the mouse neocortex through a chronic cranial window. *Nat. Protoc.* **4**, 1128–1144 (2009).
39. J. M. Mayrhofer *et al.*, Design and performance of an ultra-flexible two-photon microscope for in vivo research. *Biomed. Opt. Express* **6**, 4228–4237 (2015).
40. T. A. Pologruo, B. L. Sabatini, K. Svoboda, ScanImage: flexible software for operating laser scanning microscopes. *Biomed. Eng. Online* **2**, 13 (2003).
41. M. J. P. Barrett, K. D. Ferrari, J. L. Stobart, M. Holub, B. Weber, CHIPS: An extensible toolbox for cellular and hemodynamic two-photon image analysis. *Neuroinformatics* **16**, 145–147 (2018).
42. P. J. Drew, P. Blinder, G. Cauwenberghs, A. Y. Shih, D. Kleinfeld, Rapid determination of particle velocity from space-time images using the Radon transform. *J. Comput. Neurosci.* **29**, 5–11 (2010).
43. V. Kalchenko, D. Israeli, Y. Kuznetsov, A. Harmelin, Transcranial optical vascular imaging (TOVI) of cortical hemodynamics in mouse brain. *Sci. Rep.* **4**, 5839 (2014).